



Modeling intra-urban differences in thermal environments and heat stress based on local climate zones in central Wuhan

Qian Cao^{a,b}, He Huang^{a,b}, Yuning Hong^{a,b}, Xin Huang^{c,d}, Shaoqiang Wang^{a,b}, Lizhe Wang^{e,f}, Lunche Wang^{a,b,*}

^a Hunan Key Laboratory of Remote Sensing of Ecological Environment in Dongting Lake Area, School of Geography and Information Engineering, China University of Geosciences, Wuhan, 430074, China

^b Key Laboratory of Regional Ecology and Environmental Change, School of Geography and Information Engineering, China University of Geosciences, Wuhan, 430074, China

^c School of Remote Sensing and Information Engineering, Wuhan University, Wuhan, 430079, China

^d State Key Laboratory of Information Engineering in Surveying, Mapping and Remote Sensing, Wuhan University, Wuhan, 430079, China

^e School of Computer Science, China University of Geosciences, Wuhan, 430074, China

^f Hubei Key Laboratory of Intelligent Geo-Information Processing, China University of Geosciences, Wuhan, 430074, China

ARTICLE INFO

Keywords:

Urban morphology
Local climate zone
Thermal environment
Heat stress
Numerical simulation

ABSTRACT

Urban morphology exerts a strong influence on urban thermal environments, and local climate zones (LCZs) explicitly link urban morphology with microclimate. However, how temperature, humidity, and thermal comfort vary across different LCZs from a modeling perspective remains understudied. Here, we first developed a high-precision LCZs map of central Wuhan using a combination of GIS- and RS methods, and then simulated intra-urban differences in 2-m air temperature (T₂), water vapor mixing ration (Q₂), and heat index (HI) through incorporation of the LCZs map into a mesoscale model coupled with an urban canopy model. Results showed that the urban core area was dominated by the compact forms (i.e., LCZs 1–3), surrounded by the open forms (i.e., LCZs 4–6) and the natural/semi-natural types on the periphery (i.e., LCZs D and G). The intra-urban variability of nighttime T₂ was up to 2.5 °C and daytime Q₂ up to 0.9 g/kg across LCZs of the artificial built types. The compact forms were hotter but drier than the corresponding open forms, and LCZ 9 had the lowest T₂ but highest Q₂. HI exceeded the danger line (i.e., 41 °C) during 12:00–21:00 LST across the LCZs, with the intra-urban variability of HI in the daytime smaller than in the nighttime. That is, HI was largely influenced by Q₂ in the daytime but mainly determined by T₂ in the nighttime. Findings of this study highlighted that mitigation measures should be taken to alleviate the pressure of high temperature and humidity on human thermal comfort.

1. Introduction

The former Secretary General of the United Nations stated that the future of humanity lies in cities [1]. The United Nations' report indicated that about 55% of the global population is now living in cities and the number is expected to reach 68% by 2050 (UN, 2018). Along with the rapid growth of the urban population, urban lands are expanding rapidly. The global urban extent increased at a rate of 9687 km² per year from 1985 to 2015 [2]. And the urban lands has significantly changed the surface energy budget, hydrological cycles, and planetary boundary layer height, with additional consequences for temperature, air circulation, and precipitation changes [3–5]. The most widely recognized urbanization-induced climate change is the warming of urban areas

relative to the surrounding rural areas, which is referred to as the urban heat island (UHI) effect [6–8]. The UHI effect can greatly increase thermal stress in humans, especially during heatwave events in summer, resulting in increased heat-related mortality and morbidity in urban environments [9–11]. Therefore, the UHI effect and associated human health outcomes have received great attention in the scientific community in recent decades [12–18].

In addition to the urban-rural differences in climate conditions, recent studies have shown that the intra-urban differences may be as large as the urban-rural differences [5,19–21]. For example [5], found that the intra-urban variability of air temperature, relative humidity, and wind speed within the 6th Ring Road of Beijing can be as high as 1.88 °C, 12.77%, and 1.95 m/s, respectively. This is largely attributed to

* Corresponding author. No.388 Lumo Road, Wuhan, China.

E-mail address: wang@cug.edu.cn (L. Wang).

<https://doi.org/10.1016/j.buildenv.2022.109625>

Received 25 July 2022; Received in revised form 12 September 2022; Accepted 18 September 2022

Available online 21 September 2022

0360-1323/© 2022 Elsevier Ltd. All rights reserved.

the high complexity and heterogeneity of urban landscapes, compared with other natural, semi-natural, or artificial landscapes [22]. Specifically, the intra-urban variability of microclimate arises from intra-urban differences in (1) land cover (e.g., built versus vegetated surfaces); (2) structure (e.g., spacing and dimensions of buildings); (3) fabric (e.g., physical properties of concrete, asphalt, and steel); and (4) metabolism (e.g., matter and energy flow; [23]. To better understand the relationship between urban morphology and microclimate [24], proposed the concept of local climate zones (LCZs). The LCZs emerge from the logical division of an array of urban geometric and surface cover properties, including sky view factor, aspect ratio, building surface fraction, building height, impervious/pervious surface fraction, and terrain roughness. Undoubtedly, an in-depth understanding of the relationship between urban morphology and microclimate provides insights for urban planning for climate change adaptation.

LCZs have been classified by the World Urban Database and Access Portal Tools (WUDAPT) project, which provides a global database of LCZs using supervised classification and random forest algorithm [25–27]. Currently, LCZs classification is often achieved using RS- or GIS-based methods [28]. The RS-based method includes pixel-based, object-based, and scene-based approaches, which all use spectral and texture features derived from multi-source remote sensing imagery. Advances in machine learning and image segmentation techniques have improved the accuracy of RS-based LCZs classifications [29–31]. However, the RS-based method is likely to result in ‘the same spectrum of different LCZs’ or ‘different spectra of the same LCZ’ issues [32]. The GIS-based method, by comparison, directly uses building and volunteered geographic information, which better captures urban morphological characteristics [28]. The best choice is to integrate the advantages of RS- and GIS-based methods. That is, we classified the built types of LCZs using the GIS-based method and the natural/semi-natural types of LCZs using the RS-based method [21,33,34]. However, it is found that the RS-based method accounts for the largest proportion of relevant studies (i.e., 64.3%), followed by the GIS-based method (i.e., 26.5%), while the combined method has been infrequently used in previous research (i.e., only 9.2%; [28].

LCZs are usually linked to land surface temperature (hereafter referred to as LST') to illustrate the microclimate effects due to urban landscape heterogeneity (e.g., [21,34–37]. However, LST' is usually higher than 2-m air temperature in the daytime [38]; additionally, the availability of nighttime LST' with a fine spatiotemporal resolution is limited [39]. Above all, LST' is not the temperature directly felt by the human body. Comparatively, a 2-m air temperature is a better choice for analyzing the urban microclimate and human thermal comfort in the canopy layer. In addition to temperature, humidity also has an important influence on human thermal comfort, and urban landscape patterns exert a strong influence on humidity [5,20,40]. In fact, the number of consecutive days with high humidity may be more dangerous for humans than the number of consecutive days with high temperatures [41]. Owing to limited weather stations in urban areas, the observed meteorological variables usually fail to provide sufficient spatial details for urban microclimate research [42]. Instead, numerical models can provide high-resolution, process-based meteorological outputs in a temporally and spatially seamless manner [43]. Recent studies have incorporated LCZs into micro- or meso-scale models to improve model performance and examine the intra-urban variability of thermal environments (e.g., [40,44–49]. However, these studies usually obtained LCZs directly from WUDAPT, and ignored the humidity and heat stress differences across LCZs.

With these issues in mind, our study was designed to produce a high-precision LCZs map based on a combination of the GIS and RS methods, and to investigate intra-urban variations in microclimate (i.e., air temperature and humidity) and human thermal comfort across different LCZs using an advanced mesoscale model. The study area is focused on Wuhan, the largest city in central China, which has an extremely hot and humid summer. We first established a high-precision LCZ map for the

central urban area of Wuhan based on fine-scale building data and a high-resolution land cover map. Second, the LCZ map was incorporated into the Weather Research and Forecasting (WRF) model, which was coupled with a single-layer urban canopy model (SLUCM), to simulate microclimate responses to different LCZs during a typical heatwave event. Finally, the thermal comfort of urban residents was measured using a heat stress index. The specific research objectives were as follows: (1) characterize the spatial distribution of LCZs in central Wuhan; (2) explore the variability of daytime and nighttime 2-m air temperature and humidity across different LCZs; and (3) compare the diurnal variability of heat stress across different LCZs. Finally, we provided advice on urban planning in different LCZs to improve thermal environments and human living conditions in central Wuhan.

2. Study area

Wuhan, the capital of Hubei Province, is the largest city in central China, and it supports a population of 12.45 million and presents a gross domestic production of 1561.606 billion RMB in 2020 [50]. Wuhan lies at the confluence of the Yangtze and Han rivers, and covers a total area of 8569 km² (113°41'–115°05'E, 29°58'–31°22'N; Fig. 1a). Approximately one-fourth of the total area is covered by lakes and rivers. Wuhan has a humid subtropical monsoon climate, with extremely hot and rainy summer. The daily mean 2-m air temperature during summer ranges from 26 °C to 30 °C, with approximately 25% of the summer days having maximum temperatures exceeding 35 °C [51]. The summer relative humidity is usually greater than 60%, which is largely attributed to the hundreds of inland lakes in Wuhan. Most importantly, Wuhan has experienced unprecedented urbanization over the past three decades, which is manifested in two aspects: densification and outward expansion [52]. Thus, Wuhan is an ideal location to investigate the relationship between urban landscape patterns and microclimates. Our study area is particularly focused on the central urban area of Wuhan (accounting for 11.5% of the city's total area), where the building and population density is extremely high (Fig. 1b).

3. Materials and methods

3.1. Data acquisition and processing

The data used in this study included (1) 1:2000 building vector data, (2) high-resolution land cover map, (3) urban functional zones (UFZs) map, and (4) station-based observations in central Wuhan. A detailed description of the data is provided below:

- The 1:2000 building vector data covering the central urban area of Wuhan in 2016 were provided by the Wuhan Geomatics Institute (<http://www.whkc.com/>) and contained detailed information about building footprints and floor numbers (Fig. 1b). According to the Chinese Design Code for residential buildings (i.e., GB50096-2011), we set the height of one building floor to 3 m so that the height of the buildings could be estimated.
- The land cover map corresponding to 2013 was produced by [53] based on the ZiYuan-3 high-resolution satellite data, with a spatial resolution of 2.1 m (Fig. 1c). The land cover in central Wuhan was classified into seven types, including buildings, roads, grass/shrubs, trees, water, bare soil, and the other impervious surface area (OISA). Among the land cover types, buildings and roads were extracted using building footprints and road networks, while the other types were extracted using object-oriented classification.
- The UFZs map corresponding to 2014 was developed by [53] based mainly on the point of interest (POI) density in each city block (Fig. 1d). A UFZ is an area with specific socioeconomic functions, and there were ten UFZs identified in central Wuhan. The residential, industrial, commercial, public facility, and open spaces were represented by artificial buildings and structures, while the other zones

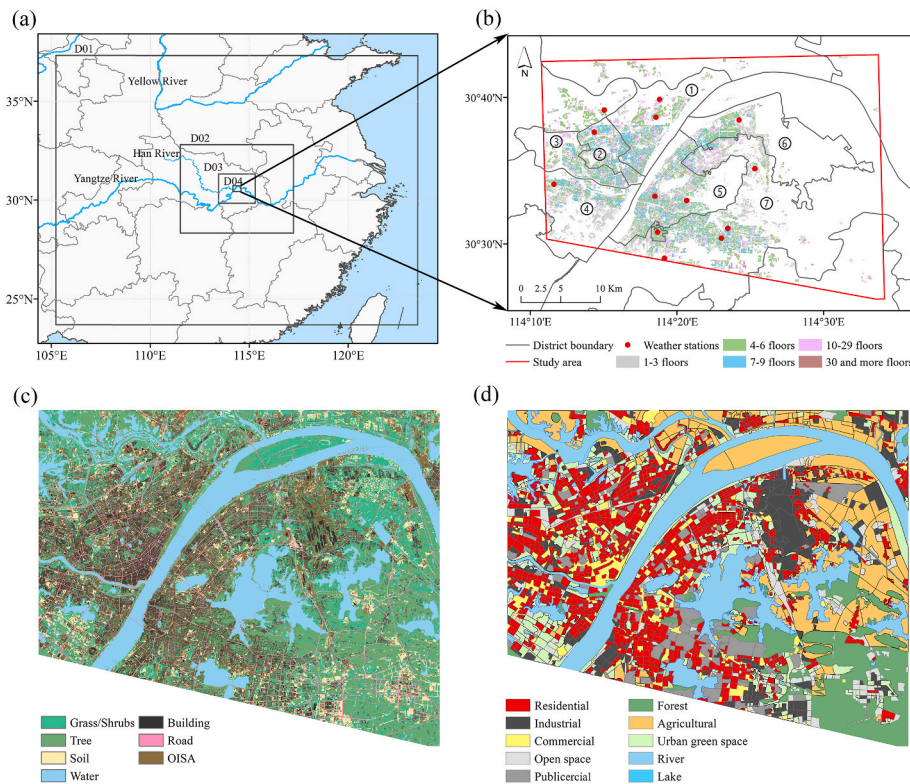


Fig. 1. Nested model domains used for the WRF simulation (a), distribution of buildings categorized by the number of floors (b), land cover map (c), and urban functional zones (d) in central Wuhan. The red dots in (b) pinpoint the automatic weather stations in the study area, and the circled numbers denote the administrative districts of Wuhan: 1-Jiang'an, 2-Jianghan, 3-Qiaokou, 4-Hanyang, 5-Wuchang, 6-Qingshan, and 7-Hongshan. OISA in (c) means other impervious surfaces. (For interpretation of the references to colour in this figure legend, the reader is referred to the Web version of this article.)

were represented by natural/semi-natural land cover. A detailed description of the ten UFZs is provided in Table S1. The UFZs map was used to explore the relationship between LCZs and UFZs because LCZs can reflect urban function to some extent according to Steward and Oke (2012).

- The hourly meteorological observations used for the model evaluation were obtained from the 13 automatic ground weather stations in the study area (Fig. 1b). These stations were deployed, operated, and maintained by the Hubei Meteorological Bureau for weather observation and forecasting (<http://hb.cma.gov.cn/>). The meteorological elements observed included a 2-m air temperature and relative humidity. To facilitate model evaluation, the simulated surface air pressure (PSFC, Pa), 2-m water vapor mixing ratio (Q2, kg/kg), and 2-m air temperature (T2, K) were used to calculate relative humidity (RH, %):

$$RH = (PSFC - 0.378 \times ES) \times Q2 / (0.62197 \times ES) \quad (1)$$

$$ES = 6.112 \times \exp(17.67 \times (T2 - 273.15) / (T2 - 29.66)) \quad (2)$$

3.2. Local climate zones mapping

According to [24]; the standard LCZs set consisted of ten artificial built types labeled as LCZs 1–10, and seven natural/semi-natural types labeled as LCZs A – G. For the artificial built types [24], used seven urban morphological parameters to classify LCZs: sky view factor (SVF), pervious surface fraction (PSF), building surface fraction (BSF), building height (BH), aspect ratio (AR), impervious surface fraction (ISF), and terrain roughness. In this study, the artificial built types were classified primarily based on architectural morphological characteristics, whereas the natural/semi-natural types were classified according to the land cover map. The specific definitions of each LCZ type identified here are presented in Tables S2 and S3, and a detailed description of how to map the artificial built types and natural/semi-natural types of LCZs in

central Wuhan is described below.

3.2.1. Artificial built types of LCZs

In this study, five out of the seven urban morphological parameters (i.e., SVF, PSF, BSF, BH, and AR) proposed by Steward and Oke (2012) and the floor area ratio (FAR) were selected to map the artificial built types of LCZs. We made additional use of FAR, which is an important parameter that was omitted from Steward and Oke (2012), because it represents building volume in a sample site. We used six parameters to represent building height, building density, building volume, and surface cover properties. Urban morphological parameters were calculated for each city blocks (i.e., streets). A detailed description of the six parameters is provided below, and the formulas used to calculate the parameters are presented in Table S4.

- BH refers to the area-weighted average height of all the buildings in a city block. We calculated the average BH, which was weighted by the building plan area in each city block. As presented earlier, the height of one floor was set to 3 m so that the heights of the buildings could be estimated. Tall buildings cooled ambient environments due to the shadowing effect on the one hand, but also led to higher temperatures due to radiation trapping on the other hand [34].
- SVF is defined as the ratio of the amount of sky hemisphere visible from ground level to that of an unobstructed hemisphere [24]. SVF affects the microclimate through incoming solar energy and ventilation in the urban canopy layer [5]. The SVF ranged from 0 (no visible sky) to 1 (no visible horizon obstructions). In this study, the SVF was calculated using the Relief Visualization Toolbox (version 2.2.1; <https://iaps.zrc-sazu.si/en/rvt>) in 32 directions with a search radius of 210 m [53].
- AR is defined as the ratio of the height to width of a street canyon [54]. Given the complex street geometry, a standardized method to calculate AR is not available. According to [54]; we calculated the AR using the area-weighted mean BH divided by the mean street width in a city block. The mean street width was estimated based on

the total street area divided by the total street length. Studies conducted in different climates have shown that the AR is positively correlated with nighttime temperatures and negatively correlated with daytime temperatures [55].

- FAR refers to the ratio of the gross floor area of a block to the block area; that is the floor area of all buildings in a block multiplied by the corresponding number of floors and divided by the total area of the block. The higher the FAR, the greater the urban load capacity. FAR is closely related to the heat capacity and anthropogenic heat emissions in urban areas. It is also one of the most important indicators of urban-land management in China [56].
- The BSF, an important parameter to distinguish compact buildings from open buildings, refers to the proportion of the gross floor area to the block area. Compared with natural/semi-natural surfaces, the presence of buildings has significantly changed the surface reflectance and heat dissipation rate [57].
- PSF is the ratio of the pervious surfaces area to the block area. Pervious surfaces, including vegetation, water, and soil, can cool the air through evaporation and/or transpiration. Thus, PSF plays a pivotal role in alleviating the UHI effect [58].

To determine the thresholds of urban morphological parameters for each LCZ of the artificial built types, we selected 20 typical samples from Google Earth (Table S2) for each LCZ and calculated the urban morphological parameters for each sample. The identified thresholds are listed in Table 1. Based on the identified thresholds, the artificial built types of LCZs were mapped according to the flowchart illustrated in Fig. S1. First, the blocks were divided into high-rise, mid-rise, and low-rise categories. For the high- and mid-rise categories, a compact morphology was distinguished from an open morphology by the addition of AR, SVF, and BSF. The high-rise category was classified into LCZs 1 and 4, whereas the mid-rise category was classified into LCZs 2, 5, and 9. The composition of the low-rise category (including LCZ 3 and LCZs 6–10) was complex. Therefore, we used PSF, BSF, and FAR to divide the low-rise category into different LCZ types. Specifically, the low-rise category was first classified into LCZ 9 and the other types using the BSF. We then distinguished LCZ 6 from the other types using the PSF. Finally, the remaining LCZ types (LCZs 3, 8, and 10) were identified using BSF and FAR.

3.2.2. Natural/semi-natural types of LCZs

The land cover map produced by [53] was used to classify the natural/semi-natural types of LCZs (i.e., LCZs A – G). We first distinguished LCZs A (dense trees), B (scattered trees), and C (bush and scrub) according to the proportion of trees and grass/shrubs in a block. That is, LCZ A was composed of more than 70% trees for the total area in a block, LCZ B was composed of 50%–70% trees, and LCZ C was mainly composed of bushes, shrubs, and short, woody trees (Table S3). Thus, we classified a city block with a proportion of grass/shrubs greater than the proportion of trees in LCZ C. LCZ D featured grass or herbaceous plants/crops, and it can be identified directly from the grass/shrubs land cover type (i.e., mostly grass/shrubs in a city block without trees). LCZ E was characterized by bare rocks or paved coverings, with few or no trees

Table 1
Thresholds of urban morphological parameters used for the LCZs classification.

LCZs	BH (m)	AR	SVF	FAR	BSF (%)	PSF (%)
LCZ1	>25	1.6–3.0	0.25–0.35	2.5–5.0	40–60	5–15
LCZ2	10–25	1.0–1.5	0.35–0.45	2.0–3.0	40–50	<20
LCZ3	<10	0.8–1.2	0.55–0.65	1.0–2.0	70–80	<10
LCZ4	>25	1.0–1.4	0.45–0.55	2.0–3.0	20–40	20–40
LCZ5	10–25	0.6–1.0	0.50–0.65	1.0–2.0	20–30	20–30
LCZ6	<10	0.2–0.6	0.60–0.70	0.5–1.0	20–30	30–40
LCZ8	<10	0.4–0.6	0.55–0.65	0.8–1.2	40–50	<20
LCZ9	3–15	0.2–0.4	0.70–0.75	0.4–0.6	10–20	>60
LCZ10	3–15	0.2–0.6	0.60–0.70	0.6–1.0	30–40	10–20

or plants, and it presented a PSF <20%. Finally, LCZs F (bare soil or sand) and G (water) corresponded to the soil and water types in the land cover map.

3.3. Numerical simulation design

The newly developed high-resolution LCZ map was incorporated into the WRF model with the advanced dynamical solver version 4.3.1 [59], so as to investigate the thermal environments of the different LCZs. The WRF model was coupled with a single-layer urban canopy model (UCM) to represent the energy and momentum exchange between the urban canopy and atmosphere [60,61]. The newest WRF-UCM (i.e., version 4.3.1) allowed for a more detailed representation of urban subcategories (compared with the previous three urban subcategories), that is, the inclusion of 11 urban subcategories corresponding to LCZs 1–10 and E into the coupled model [62]. For each identified LCZ, the BH, standard deviation of BH, roof width, road width, and urban fraction were required by the WRF-UCM (Table 2). The urban fraction (UF) was calculated by subtracting the PSF from the 1.0. The roof width and road width were calculated based on the plan area fraction (PAF) and building surface to plan area ratio (BPR) [63]:

$$PAF = A_p / A_T \quad (3)$$

$$BPR = (A_R + A_W) / A_T \quad (4)$$

where A_p is the plan area of buildings at ground level, A_R is the plan area of rooftops, A_W is the total area of nonhorizontal roughness element surfaces (e.g., walls), and A_T is the total plan area of a block. Roof width (BW) and road width (SW) were thus estimated as follows:

$$BW = 2 \times BH \times PAF / (BPR - PAF) \quad (5)$$

$$SW = 2 \times BH \times PAF \times (UF / PAF - 1) / (BPR - PAF) \quad (6)$$

The WRF model was configured with two-way, four-nested model domains, with grid spacings of 9, 3, 1, and 0.333 km from the outermost to innermost domains (Fig. 1a). The outermost domain (i.e., D01) encompasses a large proportion of China and extends into the East and South China Sea, covering a total area of 1602 km × 1494 km. The innermost domain (i.e., D04) is centered on the Wuhan City (114.37°E and 30.58°N), enclosing an area of 39 km × 33 km. A Lambert conformal conic projection was used for the model's horizontal coordinate, whereas the model's vertical coordinate employed 45 terrain-following eta levels from the surface to 50 hPa. Because the BH of LCZ 1 reached 43.6 m, we set the lowest model level to 70 m above the ground surface. The main physical parameterizations, including radiation, land surface process, cloud, convection, and boundary layer, for model simulation are presented in Table S5. Due to the large number of inland lakes in Wuhan, the CLM4.5 lake model was coupled with WRF, so as to correct for the underestimation of heat transfer between the lower and upper parts of the lakes [64]. The newly developed LCZ map for central Wuhan was then incorporated into D04 as a surface boundary condition. Note that LCZs A – D and F – G were replaced with the default land cover data provided by the WRF modeling system.

The initial and lateral boundary conditions for large-scale atmospheric fields were derived from the National Centers for Environmental Prediction (NCEP) Global Data Assimilation System (GDAS) final analysis data archive, with a horizontal resolution of 0.25° × 0.25° and a temporal interval of 6 h (<http://rda.ucar.edu/>). In addition to GDAS, we actively updated the sea surface temperature (SST) in the WRF simulation using the NCEP's real-time, global SST analysis (<ftp://polar.ncep.noaa.gov/>; RTG_SST). The RTG_SST had a grid spacing of 0.5° and a time interval of one day. To update the SST fields every 6 h, the daily SST analysis was interpolated to a time interval of 6 h and were assigned to a diurnal cycle prior to the execution of the WRF. To better capture the signal of urban landscape forcing, a clear-sky, calm-wind heatwave event in the summer of 2018 was selected as the initial and lateral

Table 2
Urban morphological parameters of LCZs used in the WRF-UCM.

	LCZ1	LCZ2	LCZ3	LCZ4	LCZ5	LCZ6	LCZ8	LCZ9	LCZ10
Building height (m)	43.6	18.3	6.2	39.4	16.7	6.1	6.5	6.0	8.3
Std. of BH ^a (m)	10.9	4.1	1.6	12.7	3.1	1.1	2.5	2.7	4.9
Roof width (m)	22.0	17.1	10.3	13.6	10.9	10.5	11.0	9.9	11.9
Road width (m)	46.0	25.5	40.3	49.3	28.9	40.0	77.9	69.0	96.8
Urban fraction (%)	0.85	0.88	0.81	0.64	0.67	0.61	0.82	0.42	0.68

^a Standard deviation of building height.

boundary conditions. The model simulation was initialized on July 18, 2018 at 00:00 UTC and terminated on July 25, 2018 at the same time. The output before July 20, 2018 at 00:00 UTC was considered as spin-up and was thus excluded from the following analysis. That is, a 5-day period (i.e., from July 20 to July 25, 2018) with a relatively stable synoptic background was used for the analysis. Finally, the simulation results for D04 were output every hour.

3.4. Heat index calculation

To evaluate human thermal comfort in different LCZs of the artificial built types, simulated T_2 and estimated RH were used to calculate the heat index (HI). The HI was calculated based on the apparent temperature to evaluate outdoor human thermal comfort, and has been widely used for meteorological heat warnings [10]. The HI is introduced as follows:

$$HI = -8.784695 + 1.61139711 \times T_2 + 2.338549 \times RH - 0.14611605 \times T_2 \times RH - 1.2308094 \times 10^{-2} \times T_2^2 - 1.6424828 \times 10^{-2} \times RH^2 + 2.211732 \times 10^{-3} \times T_2^2 \times RH + 7.2546 \times 10^{-4} \times T_2 \times RH^2 - 3.582 \times 10^{-6} \times T_2^2 \times RH^2 \quad (7)$$

where T_2 is the 2-m air temperature in °C and RH is the relative humidity in %. The HI can be divided into five thermal risk levels: 1) low risk, < 27 °C; 2) caution, 27–32 °C; 3) extreme caution, 32–41 °C; 4) danger, 41–54 °C; and 5) extreme danger, > 54 °C [10].

4. Results

4.1. Urban morphological characteristics

A set of urban morphological parameters (i.e., BH, BSF, PSF, FAR, AR, and SVF) was calculated to map the LCZs in central Wuhan (Fig. 2).

The central urban area on both sides of the Yangtze River was highly developed. Specifically, the BH was generally between 10 and 25 m, with tall buildings (i.e., >25 m) scattered across the central urban area (Fig. 2a). The BSF was greater than 0.3 in most locales, and reached 0.7 in the urban core area (Fig. 2b). Consequently, the PSF in the central urban area was generally less than 0.3 (Fig. 2c). The FAR value was closely related to the BH and BSF values. As a result, FAR was the largest in the urban core area, and decreased in the surrounding areas (Fig. 2d). Note that the area in the northeastern part (where the heavy industry was located) had a large BSF but a low FAR, because of the low BH in this region. In contrast, the AR and SVF showed no obvious regularity in terms of spatial distribution (Fig. 2e and f), because the two parameters were more comprehensive and determined by multiple factors in addition to BH and floor area. However, the SVF in the central urban area was low (i.e., less than 0.6), indicating that the openness of the urban landscape was low.

For a better recognition and understanding of the urban morphological characteristics across different LCZs of the artificial built types, we derived the ranges of BH, BSF, PSF, FAR, AR, and SVF for each LCZ type from the 20 samples obtained from Google Earth (Fig. 3). Consistent with Steward and Oke (2012), LCZs 1 and 4 belonged to high-rise buildings, LCZs 2 and 5 mid-rise buildings, and LCZs 3 and 6 low-rise buildings, while LCZs 8–10 generally consisted of low-rise buildings (Fig. 3a). The BSF of the compact category (i.e., LCZs 1–3) was larger than that of the open category (i.e., LCZs 4–6), with the compact low-rise category (i.e., LCZ 3) showing the highest BSF at between 0.7 and 0.8 (Fig. 3b). In addition, the BSF of LCZ 9 was the lowest, while those of LCZs 8 and 10 fell between the compact and open categories. The variability of the PSF was opposite to that of the BSF; however, the PSF of the same category (i.e., compact or open) was similar (Fig. 3c). Because the PSF of the high-rise categories had more paved roads, squares, etc. than the low-rise categories. The FAR and AR showed a

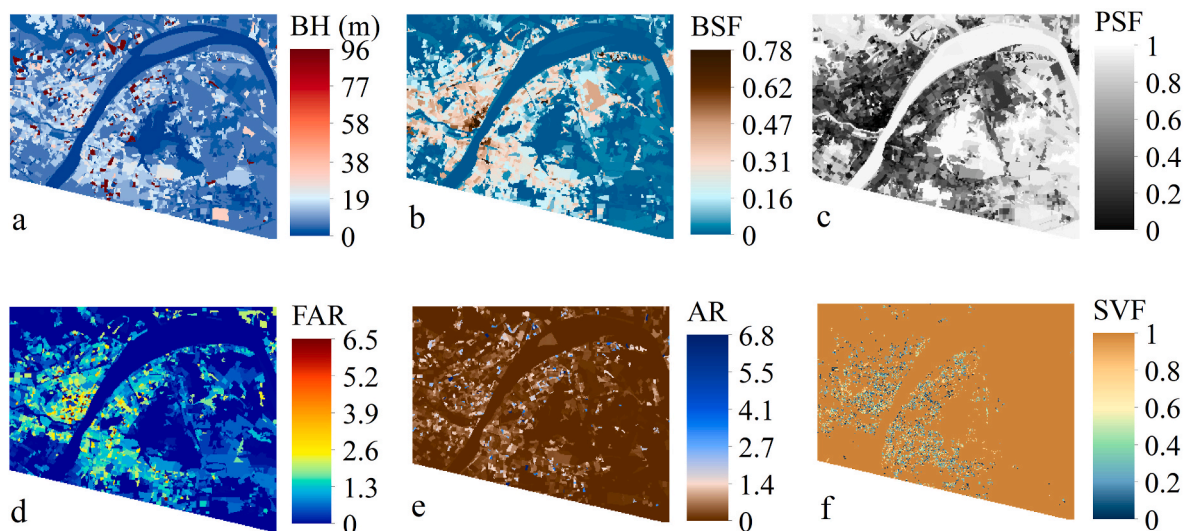


Fig. 2. Spatial patterns of urban morphological parameters used for the LCZs classification in central Wuhan: (a) building height, (b) building surface fraction, (c) pervious surface fraction, (d) floor area ratio, (e) aspect ratio, and (f) sky view factor.

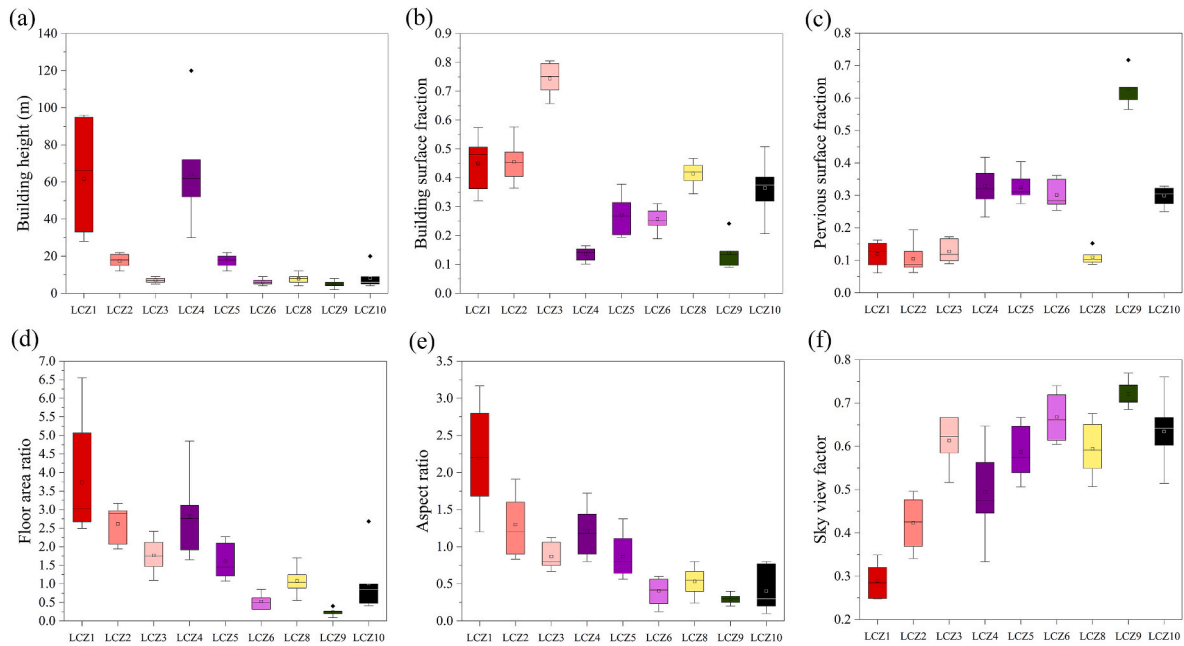


Fig. 3. Box-and-whisker plots of urban morphological parameters in LCZs of the artificial built types. The box-and-whisker plots show the maximum, minimum, median, mean (as indicated by the square dots), upper, and lower quartiles of a specific parameter.

decreasing trend within the same category, and the compact LCZ type was larger than the corresponding open LCZ type (e.g., LCZ 1 versus LCZ 4; Fig. 3d and e). Again, the FAR and AR of LCZ 9 were the lowest, followed by LCZ 6, whereas those of LCZs 8 and 10 were slightly higher than those of LCZ 6. The SVF of the same category showed an increasing trend, and the compact category was generally smaller than the open category (Fig. 3f). Exceptions were found in LCZ 3, which showed a larger SVF than LCZs 4 and 5. This meant that the BH had a significant impact on the SVF. In addition, the SVF showed an increasing trend with a decline in the FAR.

4.2. Spatial distribution pattern of LCZs

Prior to the analysis, the accuracy of our LCZ classification was assessed using the confusion matrix, with detailed information presented in Supplementary Text S1. The spatial distribution of the LCZs in central Wuhan exhibited a radial pattern (Fig. 4). That is, the innermost

urban core area along both sides of the Yangtze River belonged to the compact form (i.e., LCZs 1–3), the surrounding areas away from the urban core area belonged to the open form (i.e., LCZs 4–6), and areas at the periphery belonged to the natural/semi-natural types (i.e., LCZs D and G for the most part). For the artificial built types, the open mid-rise (i.e., LCZ 5) accounted for the largest proportion, up to 36.6% (Fig. 5a). This meant that central Wuhan was dominated by mid-rise buildings. Low-rise buildings (i.e., LCZs 3 and 6) accounted for 12.5%, while high-rise buildings (i.e., LCZs 1 and 4) only accounted for 6.2%. In addition, the heavy industry (i.e., LCZ 10) and sparsely built (i.e., LCZ 9) accounted for 17.8% and 14.0% of the artificial built types, respectively. The heavy industry (e.g., steelworks and energy groups) was mainly located in the northeastern part. The sparsely built (e.g., villages in urban and rural areas) was either scattered across the highly developed central urban area or surrounded by natural/semi-natural land cover. For the natural/semi-natural LCZ types, water (i.e., LCZ G) had the largest proportion (i.e., 34.8%), because Wuhan owned plenty of inland

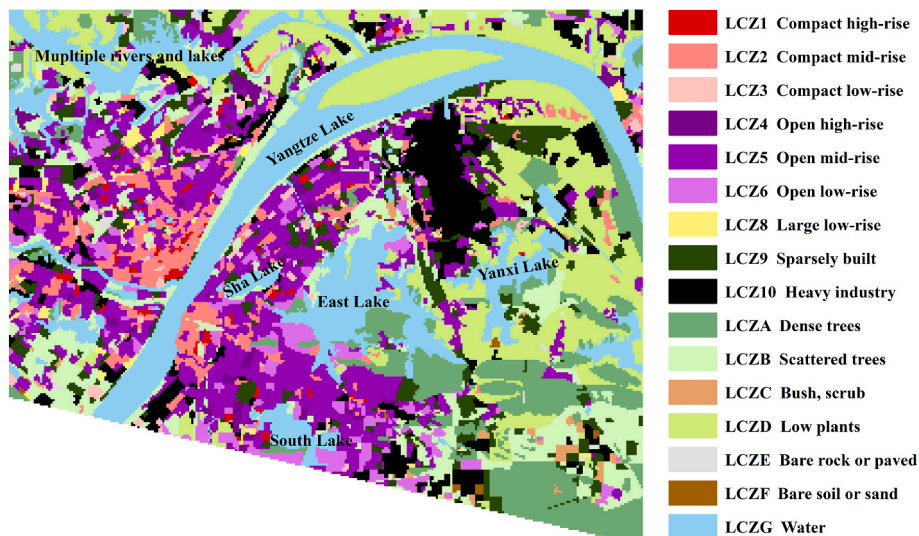


Fig. 4. Spatial distribution of LCZs in central Wuhan. LCZs 1–10 belong to the artificial built types, and LCZs A–G belong to the natural/semi-natural types.

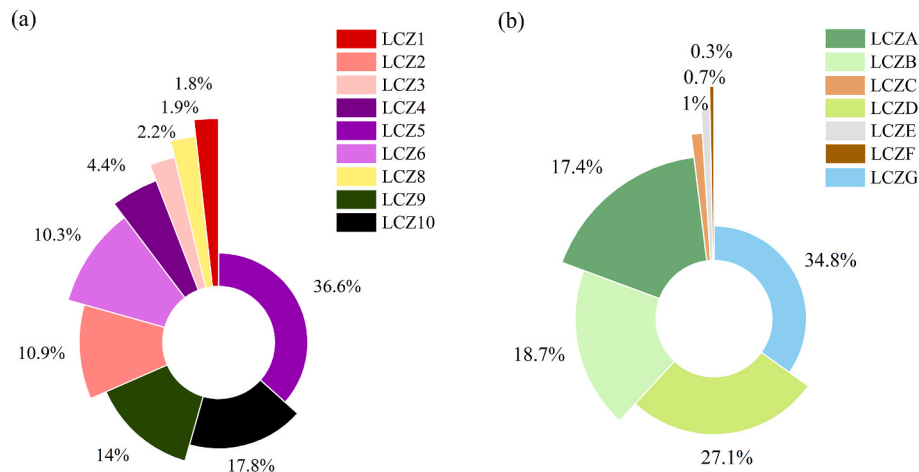


Fig. 5. The proportion of different LCZs of the artificial built types (a) and of the natural/semi-natural types (b) in central Wuhan.

lakes and rivers, including the Yangtze River, East Lake, South Lake, Sha Lake, and Yanxi Lake in our domain (Fig. 5b). The low plants (i.e., LCZ D), scattered trees (i.e., LCZ B), and dense trees (i.e., LCZ A) accounted for 27.1%, 18.7%, and 17.4%, respectively. The remaining three LCZ types (i.e., C, E, and F) accounted for only 2.0% of the natural/semi-natural types.

Next, we evaluated the proportion of different LCZs in each UFZ, that is, the connection between LCZs and UFZs. We found that the residential, commercial, and public-service UFZs were mainly composed of LCZs 1–6 (Fig. 6a). However, the proportions of LCZs 1–6 in the three UFZs varied considerably. In the residential zone, LCZ 5 (open mid-rise) accounted for 62.7%, followed by LCZ 2 (compact mid-rise) at 20.1% (Fig. 6b). However, in the commercial zone, LCZ 2 became the dominant type, followed by LCZs 5 and 6 (open low-rise). In the public-service

zone, LCZ 5 became the dominant type again (accounting for 52.3%), supplemented by LCZ 6 (accounting for 29.9%). As expected, LCZ 10, which belongs to the heavy industry, accounted for 82.2% of the industrial UFZ. LCZ 9 (sparsely built) was mainly found in the open-space UFZ. For the natural/semi-natural types, LCZs A (dense trees) and B (scattered trees) were mainly concentrated in forest and urban green space UFZs, respectively. Notably, LCZ C (bush and scrub) was infrequently found in central Wuhan. LCZ D featured grass or herbaceous plants/crops, and mainly appeared in the agricultural UFZ, with a small portion found in the urban green space UFZ. LCZs E and F accounted for a small proportion and were mainly found in the open-space UFZ.

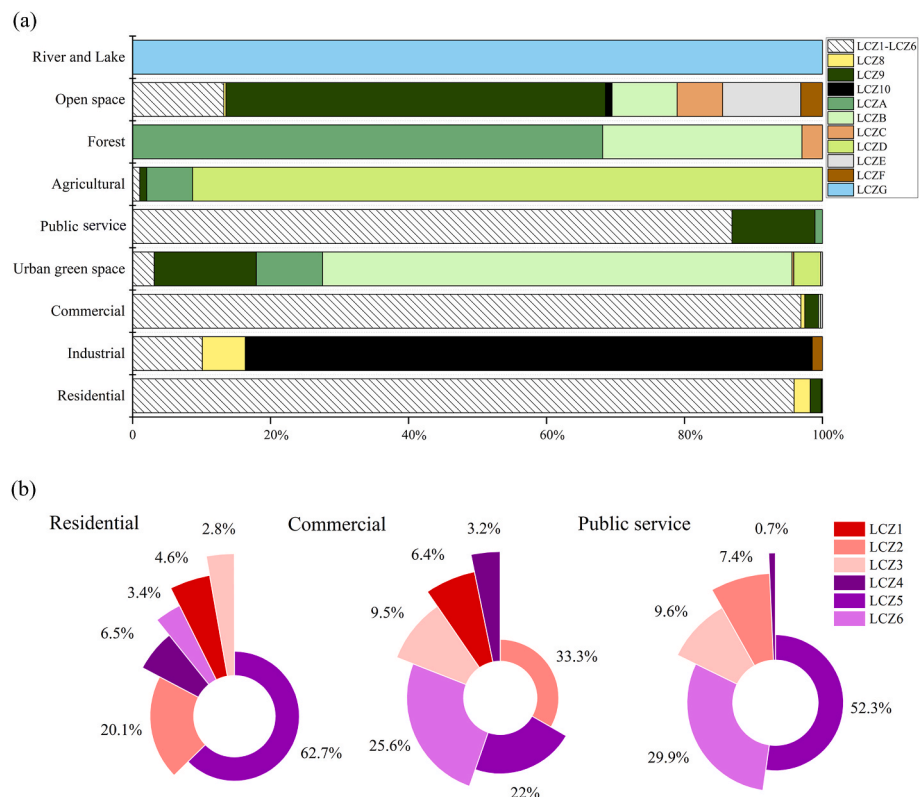


Fig. 6. Stacked column charts of the proportion of different LCZs in each urban functional zone (a) and the proportion of LCZs 1–6 in the residential, commercial, and public-service urban functional zones (b). Note that the river and lake zones are merged into one category in (a).

4.3. Thermal environments of different LCZs

The simulated 2-m air temperature (T2) and water vapor mixing ratio (Q2) using the high-resolution LCZ map as a surface boundary condition were selected to investigate the thermal environments of different LCZs in central Wuhan. The model evaluation showed that the simulation results were consistent with the observations (Supplementary Text S2). We particularly focused on the artificial built types, where human activities were held. As shown in Fig. 7, the magnitude and spatial pattern of T2 and Q2 varied considerably between the day and night. To be specific, the spatial variability of T2 was small in the daytime (i.e., generally between 34.0 °C and 35.5 °C); however, the nighttime T2 displayed a large spatial variability, with high values (i.e., approximately 33.0 °C) simulated in the urban core area and low values (i.e., 29.2–31.5 °C) around lakes and natural/semi-natural land cover. The magnitude of Q2 in the daytime (i.e., generally between 17.3 and 18.7 g/kg) was lower than that at night (i.e., mostly between 18.3 and 19.9 g/kg), and the spatial variability of Q2 in the daytime was also smaller than that at night. During both day and night, Q2 in the urban core area was the lowest, while Q2 around lakes and natural/semi-natural land cover was the highest.

To further analyze the spatial patterns of T2 and Q2, we conducted a directional analysis of T2 and Q2 variations across central Wuhan. Directional mapping detailed the spatial variability in different directions and distances from the center point [65]. In this application, the center point was located at 114°17'E and 30°33'N, with 16 directions (i.e., 0.01° interval) and 32 concentric rings from the center point. The results showed that T2 and Q2 varied more at night than during the day (Fig. 8). At night, the lowest T2 was found between the east and southeast directions outside the 19th ring, while the highest T2 mainly appeared between the west-southwest and northeast directions inside the 8th ring. The highest Q2 was in between the east-northeast and east directions outside the 26th ring, while the lowest Q2 was mainly found between the west and north directions across all rings. Typically, Q2 was high when T2 was low in most locations, and vice versa. In addition, the spatial variability of T2 and Q2 between the northeast and southeast directions was greater than the other directors owing to the complex LCZ composition.

To specify such differences in the thermal environments, we further derived T2 and Q2 from different LCZs of the artificial built types. During the daytime, for both the compact and open categories, T2 and

Q2 tended to increase as the BH decreased (Fig. 9). The T2 of the open form was slightly lower than that of the corresponding compact form during the daytime. By comparison, Q2 of the open forms was overall larger than that of the compact forms, with an average difference between the corresponding compact and open forms (e.g., LCZs 1 versus 4) of approximately 0.3 g/kg. Across the LCZs, the daytime Q2 in the compact category was the lowest (i.e., generally less than 17.6 g/kg), while daytime Q2 in LCZ 9 was much higher than the other artificial built types (i.e., 18.0–18.7 g/kg). At night, the variability of T2 and Q2 across different LCZs and the range of T2 and Q2 in a specific LCZ were larger than those in the daytime, particularly for T2. However, the differentiation of T2 and Q2 between different LCZs in the nighttime was smaller than that in the daytime. For T2, the variability pattern at night was different from that during the day. For both the compact and open categories, low-rise buildings had the lowest T2, and the compact low-rise buildings (i.e., LCZ 3) were significantly warmer than the open low-rise buildings (i.e., LCZ 6). The maximum T2 was found in LCZ 2 (i.e., 32.7 °C), followed by LCZ 1 (i.e., 32.6 °C), while the minimum was found in LCZ 9 (i.e., 30.1 °C) at nighttime. That is, the intra-urban variability of nighttime T2 was as large as 2.5 °C. The variability pattern of Q2 in the nighttime was generally consistent with that in the daytime, and the intra-urban variability of daytime Q2 was as high as 0.9 g/kg. Note that the thermal environments in LCZ 10 were close to those in LCZ 6.

The diurnal variations in T2 and Q2 for each LCZ of the artificial built types are shown in Fig. 10. Across the LCZs, the lowest T2 was found around 5:00–6:00 LST, whereas the highest value appeared around 16:00–17:00 LST (Fig. 10a). T2 was similar in all the LCZs from 8:00 to 14:00 LST. The diurnal variability of T2 in LCZs 6, 9, and 10 was larger than that of the other artificial built types, with the maximum diurnal temperature differences up to 7.0, 8.0, and 6.8 °C, respectively. This was particularly true for LCZ 9, with T2 being much lower than the other types between 18:00 and 6:00 LST. The diurnal variability of Q2 was opposite to that of T2, and a higher T2 usually led to a lower Q2 (Fig. 10b). The highest Q2 occurred around 6:00–7:00 LST, whereas the lowest value was found around 14:00–15:00 LST. Notably, Q2 showed a sharp decrease from 7:00 to 12:00 LST as T2 increased, and was relatively stable from 12:00 to 18:00 LST when T2 fluctuated in a small range. In particular, Q2 was 0.4–0.8 g/kg higher in LCZ 9 than in the other artificial built types.

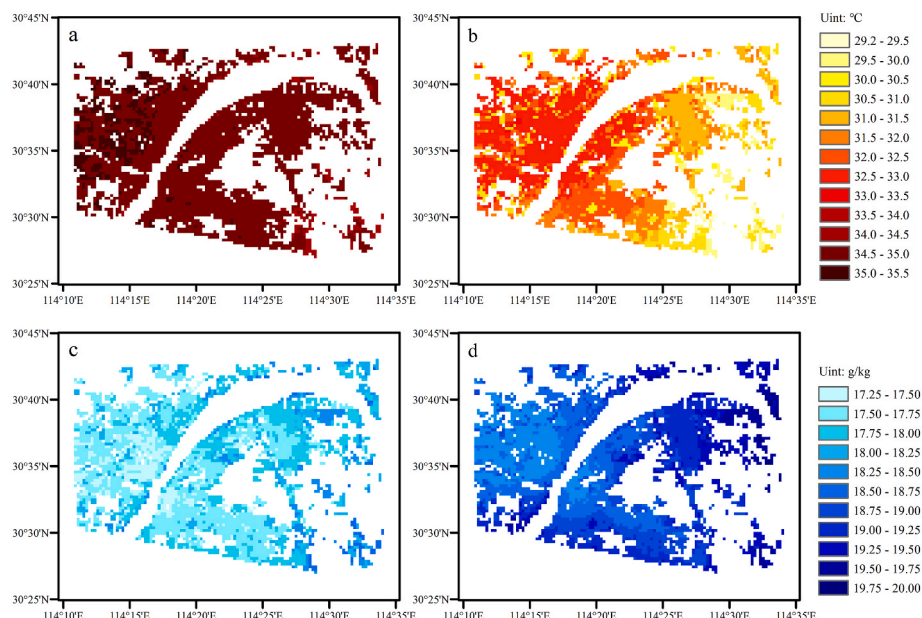


Fig. 7. Spatial patterns of simulated 2-m air temperature and water vapor mixing ratio in the daytime (a and c) and nighttime (b and d) in central Wuhan.

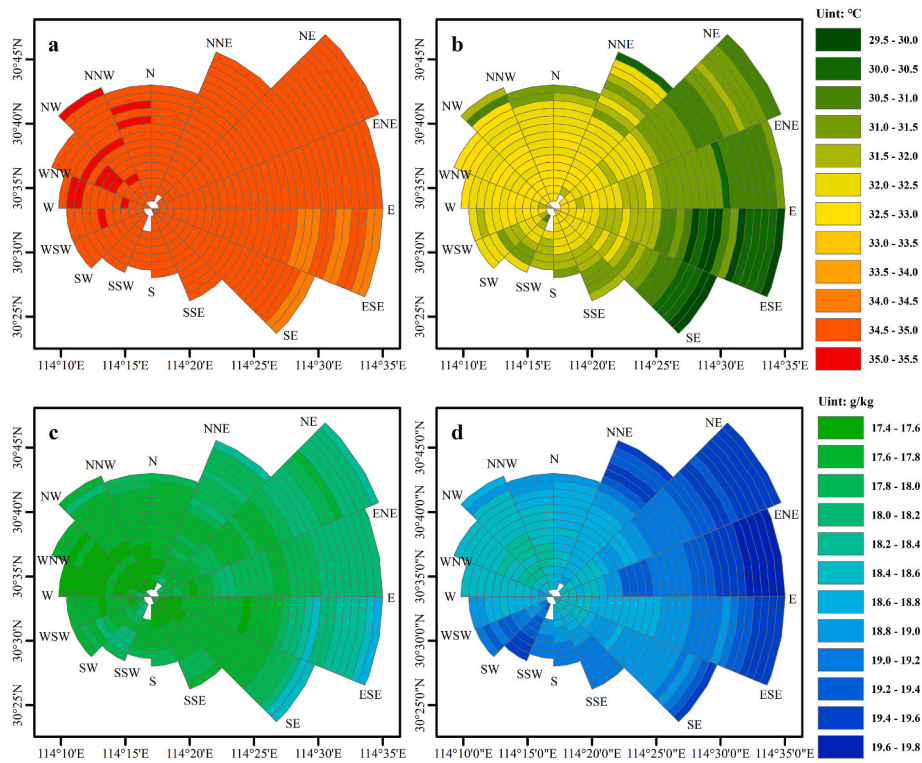


Fig. 8. Directional changes of 2-m air temperature and water vapor mixing ratio in the daytime (a and c) and nighttime (b and d) in central Wuhan.

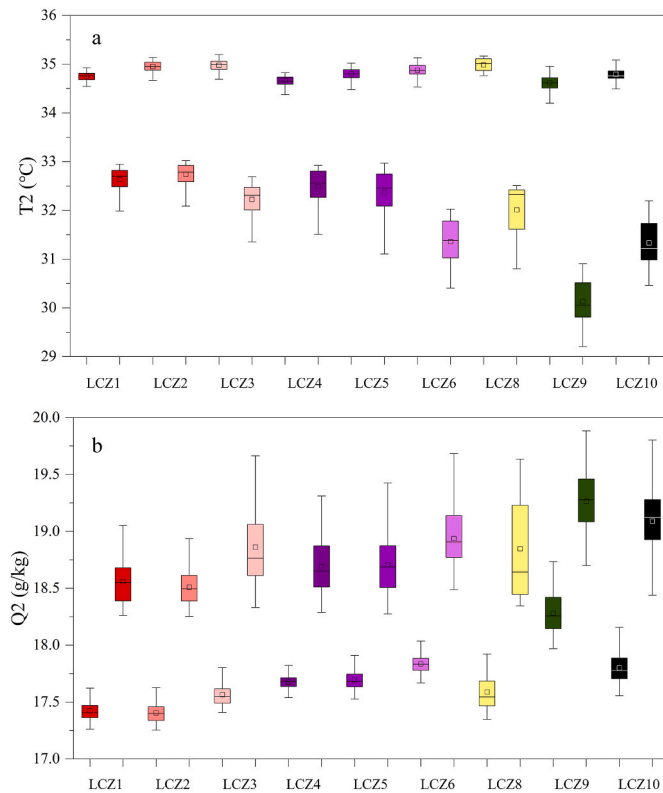


Fig. 9. Box-and-whisker plots of 2-m air temperature (T2; a) and water vapor mixing ratio (Q2; b) in LCZs of the artificial built types. The left of the box pair within each LCZ category represents daytime, while the right of the box pair represents nighttime.

4.4. Thermal comfort of different LCZs

We next evaluated human thermal comfort in LCZs of the artificial built types. We first selected four representative moments (i.e., 03:00, 09:00, 15:00, and 21:00 LST) to illustrate the spatial variability of the HI throughout the day (Fig. 11). The highest HI appeared around 15:00 LST, with a magnitude of 40.9–43.1 °C. The spatial pattern of HI at 09:00 LST, though with a reduced magnitude (i.e., 37.8–39.7 °C), was similar to that at 15:00 LST. In other words, the HI around lakes and natural/semi-natural land cover was higher than that in other areas, indicating that humidity might play an important role in regulating human thermal comfort. The lowest HI occurred at approximately 03:00 LST (i.e., 31.5–38.5 °C). Similarly, the spatial pattern of HI at 21:00 LST was similar to that at 03:00 LST, and the magnitude of HI at 21:00 LST (i.e., 37.2–42.1 °C) was second only to that at 15:00 LST. At these two moments, however, the HI along both sides of the Yangtze River (i.e., the highly developed built-up areas) was higher than that around lakes and natural/semi-natural land cover.

Indeed, the HI across the LCZs was largely influenced by humidity in the daytime, while the variability pattern of nighttime HI was greatly influenced by temperatures (Fig. 12). In the daytime, the HI of the compact form was significantly lower than that of the corresponding open form by 0.2 °C due to the drier environments of the compact form. Within the same category, the HI increased as the BH decreased. The HI in LCZ 9 was the largest (i.e., 41.0 °C on average) because of its high humidity, while the HI of LCZ 1 was the lowest (i.e., 40.3 °C on average). In the nighttime, the variability of HI across different LCZs was generally consistent with T2, with low-rise buildings having the lowest HI for both the compact and open categories. Again, the nighttime HI in LCZ 9 was much lower than that of the other artificial built types (i.e., 35.8 °C on average), and the intra-urban variability of HI reached 3.0 °C at night. Across the day, the largest difference between daytime and nighttime HI was found in LCZ 9, whereas the smallest difference appeared in LCZ 1.

The diurnal variations in the HI for each LCZ of the artificial built types are shown in Fig. 13. Clearly, nighttime HI was mainly determined

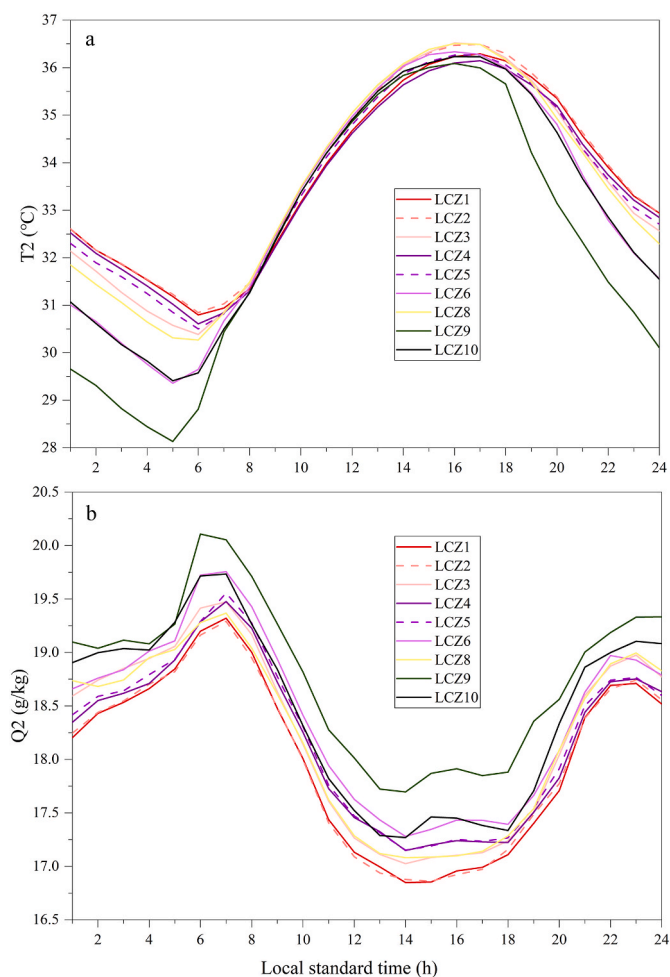


Fig. 10. Diurnal variations of 2-m air temperature (T_2 ; a) and water vapor mixing ratio (Q_2 ; b) in LCZs of the artificial built types.

by nighttime T_2 , whereas differences in daytime HI across the LCZs were due to differences in daytime Q_2 . The lowest HI was found at 5:00–6:00 LST and the highest HI was found at 16:00–17:00 LST, which was consistent with T_2 . In addition, the diurnal variability of HI in LCZs 6, 9, and 10, was larger than that of the other artificial built types, especially for LCZ 9. Across the day, the diurnal range of HI in LCZ 9 was as high as 9.9 °C, followed by LCZ 6 (i.e., 7.7 °C) and LCZ 10 (i.e., 7.4 °C), while the HI in the other LCZs was generally between 36 °C and 42 °C. Overall, the HI exceeded the danger line (i.e., >41 °C) from 12:00 to 21:00 LST, with the rest of the day falling between the extreme caution and danger lines (i.e., 32–41 °C). Within the same category (i.e., the compact or open category), the moment exceeding the danger line was delayed as the BH increased. Overall, the duration of thermal risk at the dangerous level was approximately 7–8 h across all LCZs, with low-rise buildings having a longer duration than high-rise buildings for either the compact or open category.

5. Discussion

5.1. Mapping LCZs in central Wuhan

Our LCZ map of central Wuhan was developed using GIS- and RS-based methods, with city blocks as the basic classification unit. Compared with the LCZ map from WUDAPT [26], the overall accuracy increased from 78.84% to 82.21% and the Kappa coefficient increased from 0.72 to 0.80. The discrepancies between the two LCZ maps are shown in Supplementary Fig. S2. In detail, the urban core area along

both sides of the Yangtze River was mainly classified into the compact forms (i.e., LCZs 1–3 in our LCZ map; however, the heavy industry (i.e., LCZ 10) was wrongly found here in the LCZ map of WUDAPT. For the natural/semi-natural types, areas around the Yanxi Lake were classified as LCZ D rather than LCZ B in our map, which was validated using high-resolution imagery obtained from Google Earth. Further, the southeastern corner of the domain should be dense and scattered trees (i.e., LCZs A and B), whereas it was classified as bush and scrub (i.e., LCZ C) by the WUDAPT. Previous studies have reported that LCZ C is infrequently found in central Wuhan [66–68]. In addition, the multiple rivers and lakes in the northwestern part of the domain were not identified by the WUDAPT. However, our LCZ map did not fully identify LCZ 8 (i.e., large low-rise), which was usually found on the city periphery or in a central/outlying transportation port/terminal [69]. This was because we did not select adequate samples for large shopping malls, transport hubs, or light warehouses.

Compared with the other LCZs, the classification accuracies of LCZs 6, 8, and 10 were relatively low, because urban morphological parameters of LCZs 6, 8, and 10 were close and difficult to distinguish (Supplementary Text S1 and Fig. S3). Previous studies, using both the GIS- and RS-based methods, also found that the classification accuracies of LCZs 6, 8, and 10 were relatively lower than those of other LCZ types [33,36,70]. Of the 17 standard LCZ types, two were defined by construction materials and anthropogenic heat emissions (i.e., LCZs 7 and 10, respectively; Steward and Oke, 2012). Future research should take these factors into account to better distinguish different LCZ types. For the natural/semi-natural types, the use of multi-seasonal data may help increase the classification accuracy [30,68]. For example [30], suggested that the use of multi-seasonal remote sensing imagery increased the overall accuracy from 77.9% to 79.8% and the Kappa coefficient from 0.74 to 0.76 for LCZs classification in seven European cities. LCZs have been established based on urban landscapes worldwide. Hence, not all LCZ types are found in Chinese cities. For example, the lightweight low-rise type (i.e., LCZ 7 represented by informal settlements and shantytowns) is poorly represented in China. Moreover, urban landscapes in China are highly heterogeneous and complex and are not fully characterized by standard LCZs. For example, a mix of high-rise and mid-rise buildings in a city block is common in China. The current LCZ classification must be refined to include subcategories that represent mixed types (Steward and Oke, 2012; [71,72]. Finally, the selection of samples for accuracy assessment is subjective to some extent, and [73] suggested using temperatures to evaluate LCZ classification results.

5.2. Thermal environments of different LCZs

The thermal environments and human thermal comfort of LCZs of the artificial built types were examined through the assessment of the T_2 , Q_2 , and heat index values. According to previous research, daytime LST' in the compact built form was usually higher than that in the corresponding open form in Wuhan in summer time [37,67,74], which is consistent with our results. This may be due to the lack of public spaces and green areas in compact forms compared with open forms. However, differences in daytime LST' across LCZs 1–6 (i.e., approximately 1.1 °C on average [37,67]; were greater than the differences in T_2 , as revealed by our results (i.e., approximately 0.3 °C on average). The greater differences in daytime LST' across the LCZs were mainly because LST' was much higher than T_2 during the daytime [38]. In addition, LST' is obtained at a given moment (i.e., when satellites pass through) and represents a directional parameter that differs from the simulated T_2 . The highest daytime LST' was often found in LCZs 3 or 8, and the lowest daytime LST' was found in LCZ 9 [37,67,74], which also agreed with our results. However [37], found that within the same category (i.e., the compact or open category), taller buildings led to higher LST' , which is inconsistent with our study results. In fact, high-rise buildings could lower air temperatures due to shadowing, radiation trapping, and enhanced convective heat dissipation in the daytime, but lead to higher

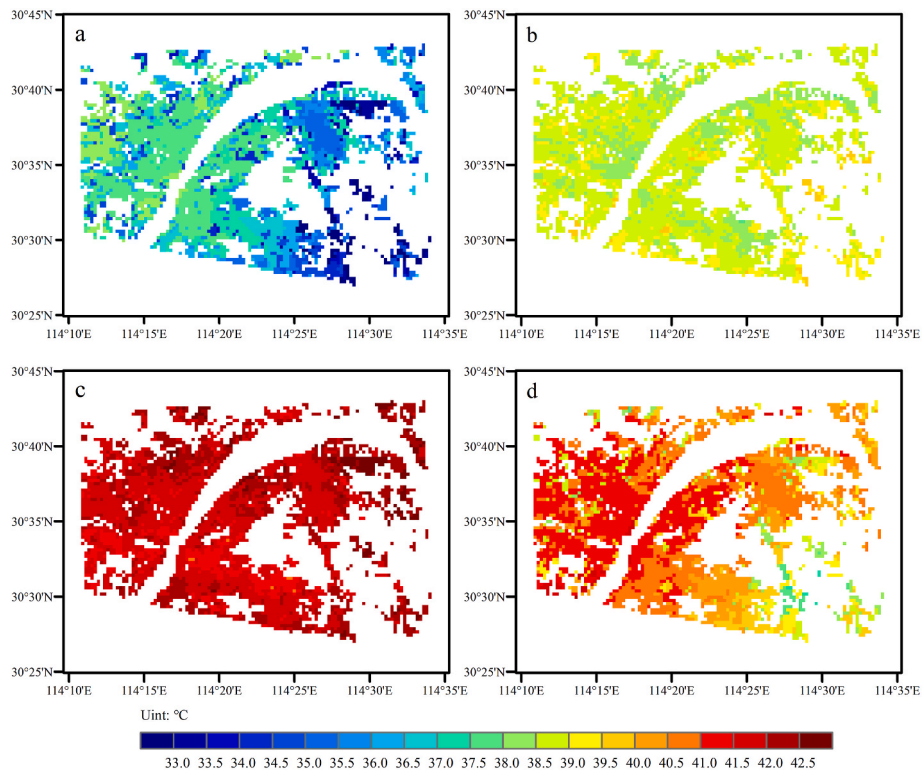


Fig. 11. Spatial patterns of simulated heat index at (a) 03:00 LST, (b) 09:00 LST, (c) 15:00 LST, and (d) 21:00 LST in central Wuhan.

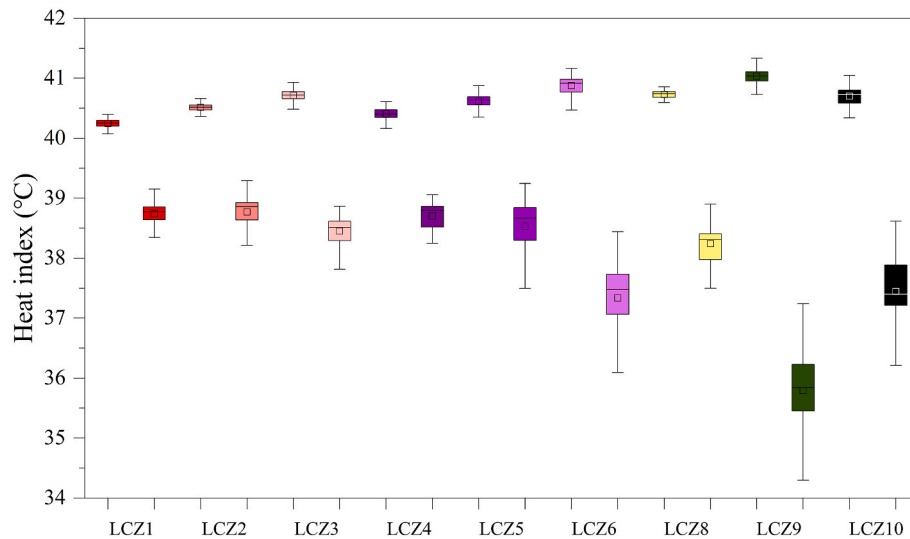


Fig. 12. Box-and-whisker plots of heat index in LCZs of the artificial built types. The left of the box pair within each LCZ category represents daytime heat index, while the right of the box pair represents nighttime heat index.

temperatures due to energy release at night [19,53,75]. Unfortunately, few studies have shown the relationship between LCZs and T2 in Wuhan, China.

Recently, an increasing number of studies have used the WRF model coupled with different land surface and urban models to evaluate model performance with enhanced urban representation (e.g., [45,46,48,76]. These studies reported that the WRF-SLUCM, which incorporates refined urban classifications (i.e., LCZs instead of the previous three sub-categories), was able to capture the spatiotemporal variations of observations, but did not necessarily improve model performance compared with the default urban representation [48,76]. Nevertheless, research with explicit consideration of the relationship between

meteorological variables and LCZs is still lacking, and few studies have fully analyzed the thermal environmental differences in T2 and Q2 across the artificial built types of LCZs, as detailed in this study. [40]; using the WRF model coupled with a multi-layer UCM (BEP) and a building energy model (BEM), found that differences in T2 across LCZs of the artificial built types were considerable from 10:00 to 18:00 LST in Hong Kong over a typical heatwave event (i.e., June 23 – June 28, 2016). In addition, the T2 in the compact form was significantly larger than that in the open form [40]. The discrepancies were likely due to the fact that we mainly focused on the effects of urban morphology on the microclimate and did not turn on anthropogenic heat release in the SLUCM, while the BEP/BEM considered the energy consumptions of

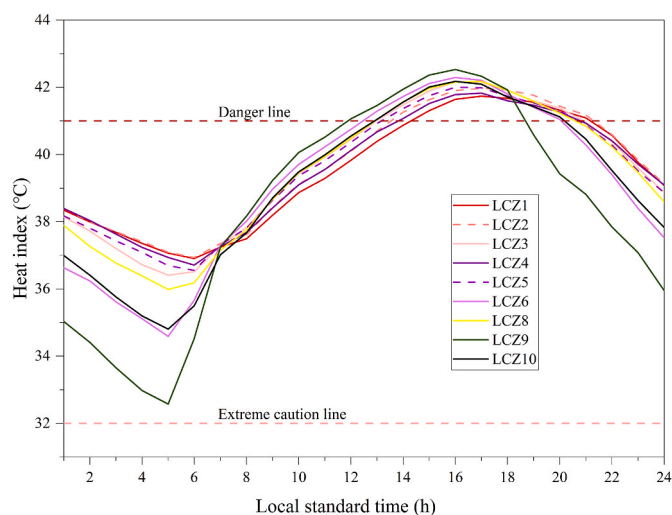


Fig. 13. Diurnal variations of heat index in LCZs of the artificial built types. The pink and red dotted lines represent the extreme caution (HI = 32 °C) and danger (HI = 41 °C) lines. (For interpretation of the references to colour in this figure legend, the reader is referred to the Web version of this article.)

buildings [77].

High air temperatures lead to severe thermal stress by restraining the heat dissipation of the human body [78]. In addition to air temperatures, the thermal sensitivity of the human body is significantly affected by humidity. High humidity aggravates the thermal stress by inhibiting sweating and skin evaporation [79]. Therefore, both air temperature and humidity are important factors for heat-related mortality and morbidity. This study showed that the nighttime HI in the compact form was larger than that in the corresponding open form, which is consistent with previous research [40,80]. This is related to the higher T2 values of the compact form at night. In addition, the HI in LCZ 9 was the highest during the daytime because the sparsely built areas were the wettest. As the HI exceeded the danger line during the daytime (i.e., very uncomfortable to be outdoors; [10], adaptation strategies should be developed for different types of LCZs (Table S6). For both the compact and open categories, the deployment of highly reflective roofs is a practical way to lower daytime HI through the reduction of air temperatures and moisture [81,82]. For the compact built types, green roofs may also be considered, depending on the dominant process that drives changes in HI (i.e., to lower HI through the reduction of air temperatures or to raise HI through the increase in moisture). For the open built types, it is also suitable to add shading devices for residents to improve outdoor daytime thermal comfort [83], because vegetation will further increase humidity in this extremely humid city. In the sparsely built areas, ventilation (e.g., air corridors) should be enhanced and people should rearrange massive outdoor activities during high-thermal-risk days. Public services and facilities (e.g., cooling spaces, heat health warning systems, emergency diagnosis and treatment) should be improved in these areas. Recent research suggests that the integration of innovative phase change materials into facades, roofs, floors, and windows is a promising alternative [78]. In addition, permeable pavements (e.g., permeable concrete and porous asphalt) are effective in reducing air temperatures [84]. However, the impact of these adaptation strategies on humidity requires further investigation. Finally, this study used the HI to measure the joint effects of T2 and Q2 on human thermal comfort; however, winds and solar radiation may also play an important role. Future research should include more meteorological factors for thermal risk assessment.

5.3. Representation of urban landscapes in the WRF-UCM

Urban landscapes are characterized by high spatial heterogeneity, which in turn affects the transfers of energy and momentum between the

urban canopy and overlying atmosphere [85]. In this study, a high-resolution LCZ map in central Wuhan was incorporated into the WRF-SLUCM as a surface boundary condition to simulate intra-urban differences in thermal environments and human thermal comfort. Although the proposed method represents a step forward in the representation of urban landscape heterogeneity for mesoscale modeling, the current urban morphological parameters of LCZs in the WRF-UCM are limited (i.e., BH, roof/road width, and UF). For these parameters, the urban fraction had the largest effect on the microclimate, followed by the BH. Thus, the simulated thermal environments in LCZs 6 and 10 were similar. In addition to the UF and BH, studies have shown that urban morphological parameters, such as AR, SVF, and FAR (i.e., the parameters used for LCZ classification), would also exert a strong influence on the urban microclimate [5,19,86]. Future model development should consider more representative urban morphological parameters of LCZs to improve the sensitivity of the model to underlying urban surfaces. In addition to the refined urban classifications represented by LCZs, recent studies have used grid-based urban morphological parameters (e.g., BH, frontal area index, and building plan area density) to improve the accuracy of urban forecasts (e.g., [63,87–89]. Undoubtedly, advances in numerical simulation technology and the increased availability of 3D surface data (e.g., LiDAR data) have largely facilitated pattern-process analysis towards 3D dimensions.

6. Conclusion

A high-precision LCZ map was first developed using a combination of GIS- and RS-based methods, and then incorporated into the WRF-SLUCM to assess intra-urban variability of microclimate (i.e., air temperatures and humidity) and human thermal comfort in central Wuhan. Results showed that: (1) the urban core area along both sides of the Yangtze River was dominated by the compact forms (i.e., LCZs 1–3), areas away from the urban core area were dominated by the open forms (i.e., LCZs 4–6), and the periphery was dominated by natural/semi-natural types (i.e., LCZs D and G for the most part); (2) the intra-urban variability of nighttime T2 was up to 2.5 °C and daytime Q2 up to 0.9 g/kg (note that the water vapor content of a parcel of air at 25 °C with 50% relative humidity is 10 g/kg); (3) the compact form was hotter but drier than the corresponding open form and the sparsely built type; (4) the HI was more responsive to Q2 in the daytime and was mainly determined by T2 at night; and (5) the HI exceeded the danger line (i.e., 41 °C) from 12:00 to 21:00 LST across all LCZs of the artificial built types. The findings provide authorities, policy makers, urban planners, and individuals with useful information on the development of adaptation strategies for different LCZs. For the compact category, highly reflective roofs and green roofs are applicable for reducing air temperatures. For the open category, highly reflective roofs and shading devices are useful for lowering both air temperatures and humidity. In LCZ 9, outdoor activities are frequently undertaken but public services and facilities are less developed. Thus, special attention need to be paid to substantially reduce its HI. First, the government should provide early heat health warnings and emergency diagnosis/treatment. Second, urban planners must design cooling spaces and ventilation corridors. Third, individuals should avoid strenuous outdoor activities on high-risk days. The government should also encourage and support the development of other promising adaptation strategies to help build livable cities.

CRedit authorship contribution statement

Qian Cao: Writing – review & editing, Writing – original draft, Supervision, Resources, Project administration, Methodology, Investigation, Data curation, Conceptualization. **He Huang:** Writing – original draft, Visualization, Validation, Software, Methodology, Formal analysis, Conceptualization. **Yuning Hong:** Visualization, Validation, Methodology, Investigation, Formal analysis, Conceptualization. **Xin Huang:** Resources. **Shaoqiang Wang:** Funding acquisition. **Lizhe**

Wang: Funding acquisition. **Lunche Wang:** Supervision, Resources, Project administration, Funding acquisition.

Declaration of competing interest

The authors declare that they have no known competing financial interests or personal relationships that could have appeared to influence the work reported in this paper.

Data availability

Data will be made available on request.

Acknowledgments

This study was supported by the National Natural Science Foundation of China (grants 41925007, 41771360, 41975044, 41801021, and 42101385) and the International Partnership Program of the Chinese Academy of Sciences (grant 132C35KYSB20200007).

Appendix A. Supplementary data

Supplementary data to this article can be found online at <https://doi.org/10.1016/j.buildenv.2022.109625>.

References

- [1] K. Annan, United Nations Press Release SG/SM/8261, United Nations, New York, 2002.
- [2] X. Liu, Y. Huang, X. Xu, X. Li, X. Li, P. Ciaias, P. Lin, K. Gong, A. Ziegler, A. Chen, P. Gong, J. Chen, G. Hu, Y. Chen, Q. Wu, K. Huang, L. Estes, Z. Zeng, High-spatiotemporal-resolution mapping of global urban change from 1985 to 2015, *Nat. Sustain.* 3 (2020) 564–570.
- [3] N.B. Grimm, S.H. Faeth, N.E. Golubiewski, C.L. Redman, J. Wu, X. Bai, J.M. Briggs, Global change and the ecology of cities, *Science* 319 (2008) 756–760.
- [4] M. Georgescu, Challenges associated with adaptation to future urban expansion, *J. Clim.* 28 (2015) 2544–2563.
- [5] Q. Cao, Q. Luan, Y. Liu, R. Wang, The effects of 2D and 3D building morphology on urban environments: a multi-scale analysis in the Beijing metropolitan region, *Build. Environ.* 192 (2021), 107635.
- [6] A. Brazel, P. Gober, S.J. Lee, S. Grossman-Clarke, J. Zehnder, B. Hedquist, E. Comparr, Determinants of changes in the regional urban heat island in metropolitan Phoenix (Arizona, USA) between 1990 and 2004, *Clim. Res.* 33 (2007) 171–182.
- [7] S.W. Myint, E.A. Wentz, A.J. Brazel, D.A. Quattrochi, The impact of distinct anthropogenic and vegetation features on urban warming, *Landsc. Ecol.* 28 (2013) 959–978.
- [8] T.R. Oke, G. Mills, A. Christen, J.A. Voogt, *Urban Climates*, Cambridge University Press, 2017.
- [9] Y. Sun, X. Zhang, F.W. Zwiers, L. Song, H. Wan, T. Hu, H. Yin, G. Ren, Rapid increase in the risk of extreme summer heat in Eastern China, *Nat. Clim. Change* 4 (2014) 1082–1085.
- [10] S. Cocolo, J. Kämpf, J.L. Scartezzini, D. Pearlmutter, Outdoor human comfort and thermal stress: a comprehensive review on models and standards, *Urban Clim.* 18 (2016) 33–57.
- [11] A.M. Vicedo-Cabrera, N. Scovronick, F. Sera, D. Royé, R. Schneider, A. Tobias, C. Astrom, Y. Guo, Y. Honda, D.M. Hondula, et al., The burden of heat-related mortality attributable to recent human-induced climate change, *Nat. Clim. Change* 11 (2021) 492–500.
- [12] E. Kalnay, M. Cai, Impact of urbanization and land-use change on climate, *Nature* 423 (2003) 528–531.
- [13] A. Sharma, H.J.S. Fernando, A.F. Hamlet, J.J. Hellmann, M. Barlage, F. Chen, Urban meteorological modeling using WRF: a sensitivity study, *Int. J. Climatol.* 37 (2017) 1885–1900.
- [14] M. Santamouris, Recent progress on urban overheating and heat island research. Integrated assessment of the energy, environmental, vulnerability and health impact. Synergies with the global climate change, *Energy Build.* 207 (2020), 109482.
- [15] H.L. Macintyre, C. Heaviside, X. Cai, R. Phalkey, The winter urban heat island: impacts on cold-related mortality in a highly urbanized European region for present and future climate, *Environ. Int.* 154 (2021), 106530.
- [16] M.N.H. Naim, A.A. Kafy, Assessment of urban thermal field variance index and defining the relationship between land cover and surface temperature in Chittogram city: a remote sensing and statistical approach, *Environmental Challenges* 4 (2021), 100107.
- [17] A.A. Kafy, M. Saha, A.A. Faisal, Z.A. Rahaman, M.T. Rahman, D. Liu, M.A. Fattah, A.A. Rakib, A.E. Aldousari, S.N. Rahaman, M.Z. Hasan, M.A.K. Ahasan, Predicting the impacts of land use/land cover changes on seasonal urban thermal characteristics using machine learning algorithms, *Build. Environ.* 217 (2022), 109066.
- [18] Z.A. Rahaman, A.A. Kafy, M. Saha, A.A. Rahim, A.I. Almulhim, S.N. Rahaman, M.A. Fattah, M.T. Rahman, S. Kalavani, A.A. Faisal, A.A. Rakib, Assessing the impacts of vegetation cover loss on surface temperature, urban heat island and carbon emission in Penang city, Malaysia, *Build. Environ.* 222 (2022), 109335.
- [19] Y. Tian, Y. Zhou, Y. Qian, Z. Zheng, J. Yan, The effect of urban 2D and 3D morphology on air temperature in residential neighborhoods, *Landsc. Ecol.* 34 (2019) 1161–1178.
- [20] D. Xu, D. Zhou, Y. Wang, W. Xu, Y. Yang, Field measurement study on the impacts of urban spatial indicators on urban climate in a Chinese basin and static-wind city, *Build. Environ.* 147 (2019) 482–494.
- [21] J. Yang, Y. Wang, C. Xiu, X. Xiao, J. Xia, C. Jin, Optimizing local climate zones to mitigate urban heat island effect in human settlements, *J. Clean. Prod.* 275 (2020), 123767.
- [22] J. Wu, C. He, G. Huang, D. Yu, Urban landscape ecology: past, present, and future, in: *Landscape Ecology for Sustainable Environment and Culture*, Springer, 2013, pp. 37–53.
- [23] T.R. Oke, Initial Guidance to Obtain Representative Meteorological Observations at Urban Sites, 51, World Meteorological Organization, 2004.
- [24] I.D. Stewart, T.R. Oke, Local climate zones for urban temperature studies, *Bull. Am. Meteorol. Soc.* 93 (2012) 1879–1900.
- [25] L.M. See, C. Perger, G. Mills, L. See, C. Perger, M. Duerauer, G. Mills, M. Foley, M. O. Connor, B. Bechtel, Developing a community-based worldwide urban morphology and materials database (WUDAPT) using remote sensing and crowdsourcing for improved urban climate modelling, *Joint Urban Rem. Sens. Event* (2015) 1–4.
- [26] C. Ren, Y. Xu, K. Lau, Wuhan WUDAPT Level 0 Training Data Is Licensed under CC-BY-NC-SA 4.0 by the Chinese University of Hong Kong, 2016.
- [27] J. Ching, G. Mills, B. Bechtel, L. See, J. Feddema, X. Wang, C. Ren, O. Brousseau, A. Martilli, M. Neophytou, et al., WUDAPT: an urban weather, climate, and environmental modeling infrastructure for the Anthropocene, *Bull. Am. Meteorol. Soc.* 99 (2018) 1907–1924.
- [28] S. Jiang, F. Huang, W. Zhan, B. Bechtel, Z. Liu, M. Demuzere, Y. Huang, Y. Xu, J. Quan, W. Xia, L. Ma, F. Hong, L. Jiang, J. Lai, C. Wang, F. Kong, H. Du, S. Miao, Y. Chen, X. Zhang, Mapping local climate zones: a bibliometric meta-analysis and systematic review, 2021, <https://doi.org/10.31219/osf.io/c2bez>.
- [29] B. Bechtel, L. See, G. Mills, M. Foley, Classification of local climate zones using SAR and multispectral data in an arid environment, *IEEE J. Sel. Top. Appl. Earth Obs. Rem. Sens.* 9 (2016) 3097–3105.
- [30] C. Qiu, L. Mou, M. Schmitt, X. Zhu, Local climate zone-based urban land cover classification from multi-seasonal Sentinel-2 images with a recurrent residual network, *ISPRS J. Photogrammetry Remote Sens.* 154 (2019) 151–162.
- [31] R.M. Simanjuntak, M. Kuffer, D. Reckien, Object-based image analysis to map local climate zones: the case of Bandung, Indonesia, *Appl. Geogr.* 106 (2019) 108–121.
- [32] Y. Xu, C. Ren, M. Cai, N.Y.Y. Edward, T. Wu, Classification of local climate zones using ASTER and landsat data for high-density cities, *IEEE J. Sel. Top. Appl. Earth Obs. Rem. Sens.* 10 (2017) 3397–3405.
- [33] S. He, Y. Zhang, Z. Gu, J. Su, Local climate zone classification with different source data in Xi'an, China, *Indoor Built Environ.* 28 (2019) 1190–1199.
- [34] L. Zhou, B. Yuan, F. Hu, C. Wei, X. Dang, D. Sun, Understanding the effects of 2D/3D urban morphology on land surface temperature based on local climate zones, *Build. Environ.* 208 (2021), 108578.
- [35] M. Cai, C. Ren, Y. Xu, K. Lau, R. Wang, Investigating the relationship between local climate zone and land surface temperature using an improved WUDAPT methodology—A case study of Yangtze River Delta, China, *Urban Clim.* 24 (2018) 485–502.
- [36] Y. Zhou, G. Zhang, L. Jiang, X. Chen, T. Xie, Y. Wei, L. Xu, Z. Pan, P. An, F. Lun, Mapping local climate zones and their associated heat risk issues in Beijing: based on open data, *Sustain. Cities Soc.* 74 (2021), 103174.
- [37] R. Wang, M. Wang, Z. Zhang, T. Hu, J. Xing, Z. He, X. Liu, Geographical detection of urban thermal environment based on the local climate zones: a case study in wuhan, China, *Rem. Sens.* 14 (2022) 1–24.
- [38] M. Jin, R.E. Dickinson, Land surface skin temperature climatology: benefitting from the strengths of satellite observations, *Environ. Res. Lett.* 5 (2010), 041002.
- [39] D. Zhou, J. Xiao, S. Bonafoni, C. Berger, K. Deilami, Y. Zhou, S. Frolking, R. Yao, Z. Qiao, J.A. Sobrino, Satellite remote sensing of surface urban heat islands: progress, challenges, and perspectives, *Rem. Sens.* 11 (2019) 1–36.
- [40] R. Du, J. Song, X. Huang, Q. Wang, C. Zhang, O. Brousseau, P.W. Chan, High-resolution regional modeling of urban moisture island: mechanisms and implications on thermal comfort, *Build. Environ.* 207 (2022), 108542.
- [41] M. Luo, N. Lau, Increasing human-perceived heat stress risks exacerbated by urbanization in China: a comparative study based on multiple metrics, *Earth's Future* 9 (2021), e2020EF001848.
- [42] K. Wang, S. Jiang, J. Wang, C. Zhou, X. Wang, X. Lee, Comparing the diurnal and seasonal variabilities of atmospheric and surface urban heat islands based on the Beijing urban meteorological network, *J. Geophys. Res. Atmos.* 122 (2017) 2131–2154.
- [43] M. Georgescu, M. Moustau, A. Mahalov, J. Dudhia, An alternative explanation of the semi-arid urban area “oasis effect”, *J. Geophys. Res. Atmos.* 116 (2011), D24113.
- [44] A. Middel, K. Hüb, A.J. Brazel, C.A. Martin, S. Guhathakurta, Impact of urban form and design on mid-afternoon microclimate in Phoenix Local Climate Zones, *Landsc. Urban Plann.* 122 (2014) 16–28.

- [45] O. Brousse, A. Martilli, M. Foley, G. Mills, B. Bechtel, WUDAPT, an efficient land use producing data tool for mesoscale models? Integration of urban LCZ in WRF over Madrid, *Urban Clim.* 17 (2016) 116–134.
- [46] K. Hammerberg, O. Brousse, A. Martilli, A. Mahdavi, Implications of employing detailed urban canopy parameters for mesoscale climate modelling: a comparison between WUDAPT and GIS databases over Vienna, Austria, *Int. J. Climatol.* 38 (2018) e1241–e1257.
- [47] I. McRae, F. Freedman, A. Rivera, X. Li, J. Dou, I. Cruz, C. Ren, I. Dronova, H. Fraker, R. Bornstein, Integration of the WUDAPT, WRF, and ENVI-met models to simulate extreme daytime temperature mitigation strategies in San Jose, California, *Build. Environ.* 184 (2020), 107180.
- [48] T. Liang, J. He, L. Chen, Z. Yao, L. Zhang, H. Che, S. Gong, Simulation of the influence of a fine-scale urban underlying surface on the urban heat island effect in Beijing, *Atmos. Res.* 262 (2021), 105786.
- [49] J. Ren, J. Yang, Y. Zhang, X. Xiao, J. Xia, X. Li, S. Wang, Exploring thermal comfort of urban buildings based on local climate zones, *J. Clean. Prod.* 340 (2022), 130744.
- [50] China Statistical Yearbook, Hubei Provincial Bureau, 2020 Statistics Bulletin of the National Economic and Social Development of Hubei Province, 2021.
- [51] X. Deng, Q. Cao, L. Wang, W. Wang, S. Wang, L. Wang, Understanding the impact of urban expansion and lake shrinkage on summer climate and human thermal comfort in a land-water mosaic area, *J. Geophys. Res. Atmos.* 127 (2022), e2021JD036131.
- [52] L. Jiao, T. Dong, G. Xu, Z. Zhou, J. Liu, Y. Liu, Geographic micro-process model: understanding global urban expansion from a process-oriented view, *Comput. Environ. Urban Syst.* 87 (2021), 101603.
- [53] X. Huang, Y. Wang, Investigating the effects of 3D urban morphology on the surface urban heat island effect in urban functional zones by using high-resolution remote sensing data: a case study of Wuhan, Central China, *ISPRS J. Photogrammetry Remote Sens.* 152 (2019) 119–131.
- [54] Y. Zheng, C. Ren, Y. Xu, R. Wang, J. Ho, K. Lau, E. Ng, GIS-based mapping of Local Climate Zone in the high-density city of Hong Kong, *Urban Clim.* 24 (2018) 419–448.
- [55] F. Bourbia, F. Boucheriba, Impact of street design on urban microclimate for semi arid climate (Constantine), *Renew. Energy* 35 (2010) 343–347.
- [56] H. Xu, H. Chen, X. Zhou, Y. Wu, Y. Liu, Research on the relationship between urban morphology and air temperature based on mobile measurement: a case study in Wuhan, China, *Urban Clim.* 34 (2020), 100671.
- [57] M. Das, A. Das, Assessing the relationship between local climatic zones (LCZs) and land surface temperature (LST) – a case study of Sriniketan-Santiniketan Planning Area (SSPA), West Bengal, India, *Urban Clim.* 32 (2020), 100591.
- [58] A. Sharma, P. Conry, H.J.S. Fernando, A.F. Hamlet, J.J. Hellmann, F. Chen, Green and cool roofs to mitigate urban heat island effects in the Chicago metropolitan area: evaluation with a regional climate model, *Environ. Res. Lett.* 11 (2016), 064004.
- [59] W.C. Skamarock, J.B. Klemp, J.B. Dudhia, D.O. Gill, D.M. Barker, M.G. Duda, X.-Y. Huang, W. Wang, J.G. Powers, A Description of the Advanced Research WRF Model, NCAR/TN-556+STR, 2021 (No, Version 4.3).
- [60] H. Kusaka, H. Kondo, Y. Kikegawa, F. Kimura, A simple single-layer urban canopy model for atmospheric models: comparison with multi-layer and slab models, *Boundary-Layer Meteorol.* 101 (2001) 329–358.
- [61] H. Kusaka, F. Kimura, Coupling a single-layer urban canopy model with a simple atmospheric model: impact on urban heat island simulation for an idealized case, *J. Meteorol. Soc. Jpn.* 82 (2004) 67–80.
- [62] A. Zonato, F. Chen, Updates of WRF-Urban in WRF 4.3: Local Climate Zones, Mitigation Strategies, Building Materials Permeability and New Buildings Drag Coefficient, 2021.
- [63] C. Shen, X. Chen, W. Dai, X. Li, J. Wu, Q. Fan, X. Wang, L. Zhu, P. Chan, J. Hang, S. Fan, W. Li, Impacts of high-resolution urban canopy parameters within the WRF model on dynamical and thermal fields over Guangzhou, China, *J. Appl. Meteorol. Climatol.* 58 (2019) 1155–1176.
- [64] H. Gu, J. Jin, Y. Wu, M.B. Ek, Z.M. Subin, Calibration and validation of lake surface temperature simulations with the coupled WRF-lake model, *Clim. Change* 129 (2013) 471–483.
- [65] A.A. Kafy, A.A. Rakib, K.S. Akter, Z.A. Rahaman, A.A. Faisal, S. Mallik, N.M. R. Nasher, M.I. Hossain, M.Y. Ali, Monitoring the effects of vegetation cover losses on land surface temperature dynamics using geospatial approach in Rajshahi City, Bangladesh, *Environmental Challenges* 4 (2021), 100187.
- [66] Z. Cai, Y. Tang, Q. Zhan, A cooled city? Comparing human activity changes on the impact of urban thermal environment before and after city-wide lockdown, *Build. Environ.* 195 (2021), 107729.
- [67] L. Shi, F. Ling, G.M. Foody, Z. Yang, X. Liu, Y. Du, Seasonal SUHI analysis using local climate zone classification: a case study of Wuhan, China, *Int. J. Environ. Res. Publ. Health* 18 (2021) 7242.
- [68] L. Shi, F. Ling, Local climate zone mapping using multi-source free available datasets on google earth engine platform, *Land* 10 (2021) 454.
- [69] I.D. Stewart, Redefining the Urban Heat Island (Thesis), University of British Columbia, 2011.
- [70] R. Wang, C. Ren, Y. Xu, K. Lau, Y. Shi, Mapping the local climate zones of urban areas by GIS-based and WUDAPT methods: a case study of Hong Kong, *Urban Clim.* 24 (2018) 567–576.
- [71] R. Kotharkar, A. Bagade, Local Climate Zone classification for Indian cities: a case study of Nagpur, *Urban Clim.* 24 (2018) 369–392.
- [72] X. Zhou, T. Okaze, C. Ren, M. Cai, Y. Ishida, A. Mochida, Mapping local climate zones for a Japanese large city by an extended workflow of WUDAPT Level 0 method, *Urban Clim.* 33 (2020), 100660.
- [73] I.D. Stewart, T.R. Oke, E.S. Krayenhoff, Evaluation of the “local climate zone” scheme using temperature observations and model simulations, *Int. J. Climatol.* 34 (2014) 1062–1080.
- [74] Y. Wang, Q. Zhan, W. Ouyang, Impact of Urban climate landscape patterns on land surface temperature in Wuhan, China, *Sustainability* 9 (2017) 1700.
- [75] Q. Cao, D. Yu, M. Georgescu, J. Wu, Impacts of urbanization on summer climate in China: an assessment with coupled land-atmospheric modeling, *J. Geophys. Res. Atmos.* 121 (10) (2016), 505–10,521.
- [76] G. Molnár, A.Z. Gyöngyösi, T. Gál, Integration of an LCZ-based classification into WRF to assess the intra-urban temperature pattern under a heatwave period in Szeged, Hungary, *Theor. Appl. Climatol.* 138 (2019) 1139–1158.
- [77] F. Salamanca, A. Martilli, A new Building Energy Model coupled with an Urban Canopy Parameterization for urban climate simulations-part II. Validation with one dimension off-line simulations, *Theor. Appl. Climatol.* 99 (2010) 345–356.
- [78] K.L. Kownacki, C. Gao, K. Kuklane, A. Wierzbicka, Heat stress in indoor environments of Scandinavian urban areas: a literature review, *Int. J. Environ. Res. Publ. Health* 16 (2019) 1–18.
- [79] K.L. Lee, Y.H. Chan, T.C. Lee, W.B. Goggins, E.Y.Y. Chan, The development of the Hong Kong Heat Index for enhancing the heat stress information service of the Hong Kong Observatory, *Int. J. Biometeorol.* 60 (2016) 1029–1039.
- [80] R. Kotharkar, A. Ghosh, V. Kotharkar, Estimating summertime heat stress in a tropical Indian city using Local Climate Zone (LCZ) framework, *Urban Clim.* 36 (2021), 100784.
- [81] M. Georgescu, M. Moustaooui, A. Mahalov, J. Dudhia, Summer-time climate impacts of projected megapolitan expansion in Arizona, *Nat. Clim. Change* 3 (2013) 37–41.
- [82] M. Georgescu, P.E. Morefield, B.G. Bierwagen, C.P. Weaver, Urban adaptation can roll back warming of emerging megapolitan regions, *Proc. Natl. Acad. Sci. USA* 111 (2014) 2909–2914.
- [83] H. Yan, F. Wu, X. Nan, Q. Han, F. Shao, Z. Bao, Influence of view factors on intra-urban air temperature and thermal comfort variability in a temperate city, *Sci. Total Environ.* 841 (2022), 156720.
- [84] J. Stempihar, T. Pourshams-Manzouri, K. Kaloush, M. Rodezno, Porous asphalt pavement temperature effects for urban heat island analysis, *Transport. Res. Rec.* 2293 (2012) 123–130.
- [85] J. Ching, D. Aliaga, G. Mills, V. Masson, L. See, M. Neophytou, A. Middel, A. Baklanov, C. Ren, E. Ng, et al., Pathway using WUDAPT’s Digital Synthetic City tool towards generating urban canopy parameters for multi-scale urban atmospheric modeling, *Urban Clim.* 28 (2019), 100459.
- [86] C. Berger, J. Rosentreter, M. Voltersen, C. Baumgart, C. Schmuilius, S. Hese, Spatio-temporal analysis of the relationship between 2D/3D urban site characteristics and land surface temperature, *Rem. Sens. Environ.* 193 (2017) 225–243.
- [87] X. He, Y. Li, X. Wang, L. Chen, B. Yu, Y. Zhang, S. Miao, High-resolution dataset of urban canopy parameters for Beijing and its application to the integrated WRF/Urban modelling system, *J. Clean. Prod.* 208 (2019) 373–383.
- [88] X. Zhang, G.J. Steeneveld, D. Zhou, R.J. Ronda, C. Duan, S. Koopmans, A.A. M. Holtslag, Modelling urban meteorology with increasing refinements for the complex morphology of a typical Chinese city (Xi’an), *Build. Environ.* 182 (2020), 107109.
- [89] Y. Sun, N. Zhang, S. Miao, F. Kong, Y. Zhang, N. Li, Urban morphological parameters of the main cities in China and their application in the WRF model, *J. Adv. Model. Earth Syst.* 13 (2021), e2020MS002382.